First climatology of F-region UHF echoes observed by the AMISR-14 system at the Jicamarca Radio Observatory and comparison with the climatology of VHF echoes observed by the collocated JULIA radar

Alexander A. Massoud[1], Fabiano S. Rodrigues[1], Jonas Sousasantos[1], Marco A. Milla[2], Danny E. Scipion[3], Joab M. Apaza[3], Karim M. Kuyeng[3], and Carlos Padin[4]

[1]The University of Texas at Dallas, William B. Hanson Center for Space Sciences, Richardson, TX 75080, USA
[2]Pontificia Universidad Católica del Perú, Sección Electricidad y Electrónica, Lima, Perú
[3]Instituto Geofísico del Perú, Radio Observatorio de Jicamarca, Lima, Perú
[4]Universidad Ana G. Méndez, San Juan, Puerto Rico

Corresponding author: Alexander Massoud (Alexander.Massoud@UTDallas.edu)

Abstract: Coherent backscatter radar observations made at the Jicamarca Radio Observatory (JRO) have contributed significantly to our understanding of equatorial F-region irregularities. Radar observations, however, have been made predominantly at the Very-High Frequency (VHF) band (50 MHz), which corresponds to measurements of 3-meter field-aligned irregularities. The deployment of the 14-panel version of the Advanced Modular Incoherent Scatter Radar (AMISR-14) at Jicamarca provided an opportunity for observations of Ultra-High Frequency (UHF - 445 MHz) echoes which correspond to measurements of irregularities with 0.34 m scale sizes. Here, we present what we believe to be the first report describing the quiet-time climatology of sub-meter equatorial F-region irregularities derived from UHF radar measurements. The measurements were made between August 2021 and February 2023 using a 10-beam AMISR-14 mode that scanned the F-region in the magnetic equatorial plane. The results show how F-region sub-meter irregularities respond to variations in season and solar flux conditions. The results also confirm, experimentally, that the occurrence of UHF F-region echoes is controlled by the occurrence of equatorial spread F (ESF). Higher occurrence rates were observed during pre-midnight hours and during Equinox and December solstice. Reduced occurrence rates were observed during June solstice. The results show that an increase in solar flux was followed by an increase in the altitude where noticeable occurrence rates ($\gtrsim 10\%$) start and in the maximum altitude of these occurrence rates. The observations also show that occurrence rates lasted longer (in local time) during low solar flux conditions. Comparisons with collocated VHF radar observations showed that, despite differences in radar parameters, observation days, and the scale size (one order of magnitude) of the scattering irregularities, the two systems show similar climatological variations with only minor differences in the absolute occurrence rates. Finally, the analysis of the occurrence rates for different beams did not show substantial climatological variations over local (within a few 100s of km) zonal distances around JRO. We point out, however, that observations on a single day can show strong local variations in echo detection and intensity within the AMISR-14 field of view due to the intrinsic development and decay of ESF structures.

Keywords: Ionosphere, irregularities, equatorial spread F, radar, coherent scatter, UHF, VHF

Key Points:

- We report for the first time the climatology of nighttime F-region echoes observed by a UHF radar operated at the magnetic equator.
- We present and discuss how the occurrence rate (as a function of local time and height) of the UHF echoes responds to variations in season and solar flux conditions and how these variations relate to ESF.
- We show that, despite differences in radar parameters and irregularity scale sizes, the climatology of irregularities observed by AMISR-14 is similar to that observed by the collocated VHF JULIA radar.
- The analysis of the 10-beam F-region mode observations confirms that the climatology of ESF echoes does not change within local (a few 100s of km) zonal distances.

1 Introduction

Equatorial spread F (ESF) is the name given, for historical reasons (Booker and Wells, 1938), to a broad spatial spectrum of ionospheric irregularities observed by different types of ground-based instruments including, but not limited to, ionosondes (Abdu et al., 2000), airglow photometers and imagers (Kelley et al., 2002; Martinis and Mendillo, 2007; Sekar et al., 2008), and ionospheric scintillation and total electron content (TEC) monitors (Rastogi et al., 1981; Rodrigues et al., 2004; Carrano et al., 2007; Alfonsi et al., 2013). ESF irregularities have also been observed by instruments on satellites (e.g., Hoegy et al., 1982; Thampi et al., 2009; Rodrigues et al., 2009) and rockets (e.g., Szuszczewicz et al., 1980; Rino et al., 1981; Jahn and LaBelle, 1998).

More recent studies of ESF have focused on a better understanding of the short-term (day-to-day) variability in ESF occurrence (Tsunoda, 2006; Smith et al., 2016; Abdu, 2019). Efforts have also been dedicated to studies of atypical ESF, that is, ESF events that occur outside the expected local times and/or seasons when conditions are favorable to the instability leading to ESF irregularities (Patra et al., 2009; Yizengaw et al., 2013; Otsuka, 2018; Zhan et al., 2018). Experimental progress in this area, however, requires investigations of new observational capabilities that would complement and expand existing measurements. Of relevance here are new Ultra-High Frequency (UHF) radar observations of equatorial F-region irregularities.

Coherent backscatter radar measurements made at the Jicamarca Radio Observatory (JRO) since the 1960s have contributed significantly to the current state of knowledge of ESF. Coherent radar echoes are caused by Bragg scattering of radio waves by field-aligned irregularities with transverse (to the geomagnetic field) scale sizes matching half the wavelength of the radar signal. The Jicamarca radar operates at 50 MHz and, therefore, observations are due to the scattering of radio waves by 3-meter irregularities.

The seminal work of Woodman and La Hoz (1976) highlights the contribution of the Jicamarca radar to our understanding of ESF. They presented and discussed some of the first range-time-intensity (RTI) maps obtained with the Jicamarca radar system. The power profiles in the RTI maps provide insight into the occurrence of irregularities as a function of range. The temporal variation of these profiles, on the other hand, provides information about the temporal variation of the irregularity-causing echoes within the field of view of the radar. Spaced antenna modules and interferometric radar imaging techniques were then used to investigate the spatial distribution of the irregularities (e.g., Kudeki and Sürücü, 1991; Hysell, 1996; Chau and Woodman, 2001; Harding and Milla, 2013; Rodrigues et al., 2017). However, the technique can only image the area illuminated by the radar which is, typically, only a few degrees wide in the magnetic zonal direction and, as a result, only covers a few 10s of km in the zonal direction at F-region peak heights.

In 2014, a smaller version of the Advanced Modular Incoherent Scatter Radar (AMISR) system was deployed at JRO for tests. The standard AMISR can be described as a modular, mobile radar system for radio remote sensing of the Earth's upper atmosphere and ionosphere and for studies of the space weather (e.g., Valentic et al., 2013). AMISR can operate within 430-450 MHz, in the UHF band. The initial tests with the AMISR system deployed at Jicamarca (AMISR-14) showed that it is capable of detecting coherent backscatter echoes from F-region irregularities (Hickey et

al., 2015; Rodrigues et al., 2015). Of relevance here is that observations at 445 MHz correspond to measurements of sub-meter (34 cm) ionospheric irregularities.

Due to technical issues, AMISR-14 only started semi-routine observations (~ 200 nights per year) in July 2021 when repairs to the system were completed. Rodrigues et al. (2023) presented a description of a new 10-beam mode for F-region observations and highlighted the benefits of multi-beam (two-dimensional) observations of equatorial spread F (ESF). They focused on observations made on a single night in which a wide variety of ESF events were detected including pre-midnight, post-midnight, and pre-sunrise ESF scattering layers.

Here, we present results of the fundamental next step in the analysis of the observations which consists of an investigation of the behavior of UHF F-region echoes based on a larger set of measurements. More specifically, we present and discuss the results of a statistical analysis of the geomagnetically quiet-time F-region echoes made by AMISR-14 between September equinox 2021 and December solstice 2022.

We clarify that previously reported results describing the climatology of F-region irregularities as a function of height and time at the magnetic equator come from VHF radar observations and, therefore, correspond to meter-scale irregularities. Moreover, VHF echo climatologies were mainly obtained for a single pointing direction (i.e., directly overhead). The AMISR-14 UHF measurements allow us to determine, for the first time, how the climatology of sub-meter equatorial F-region irregularities responds to variations in season and solar flux conditions. The ability of AMISR-14 to electronically steer its beam also allows us to determine zonal variations within a few 100s of km.

Additionally, being located at Jicamarca, the 445 MHz AMISR-14 observations can be compared with those obtained for meter-scale irregularities by the 50 MHz Jicamarca Unattended Long-term Investigations of the Ionosphere and Atmosphere (JULIA) radar. Given that the two radars measure irregularities with scale sizes that are significantly different (one order of magnitude apart), the comparison of collocated observations allows us to determine, for the first time, to what extent the two climatologies differ.

We highlight that the results reported here are relevant to decisions being made with respect to the development and deployment of new radar systems. Systems targeting both coherent and incoherent scatter observations could benefit from, for instance, the reduced sky noise at UHF, which is two orders of magnitude lower than the sky noise at VHF (Hysell et al., 2019). Therefore, the report contributes with information about what the climatology of equatorial F-region UHF echoes looks like and how it compares with the climatology of collocated VHF measurements. This comparison between UHF and VHF climatologies in the equatorial region is the first of its type reported.

This report is organized as follows: In Section 2, we present a brief description of AMISR-14 and of the mode used for F-region observations. In Section 3, we present and discuss results related to variations in the occurrence of UHF echoes as a function of local time and height in response to changes in season and solar flux conditions. We also compare and discuss occurrences of ESF

observed by collocated UHF and VHF radar systems. In Section 4, we summarize our results and list our main conclusions.

2 Methods: instrumentation and analyses

This study uses UHF radar measurements of sub-meter irregularities made by a 14-panel AMISR system (Valentic et al., 2013). Additionally, the UHF radar measurements made by AMISR-14 are compared with collocated VHF radar observations made by the JULIA system (Hysell and Burcham, 1998). Information about AMISR-14 and JULIA is provided below.

2.1 AMISR-14

AMISR-14 is a monostatic radar system that operates in the UHF band (445 MHz) and can electronically steer its antenna beam.

While AMISR-14 was first deployed at the JRO (11.95º S, 76.87º W, ~ 1º dip latitude) in 2014, a series of technical issues did not allow the system to operate continuously and only a few observations were made until recently. Rodrigues et al. (2015), nevertheless, were able to show that the system is capable of making measurements of nighttime sub-meter F-region irregularities associated with equatorial spread F (ESF). Repairs of the system started in 2019, and semi-routine observations of ionospheric F-region irregularities with the system began in July 2021 (Rodrigues et al., 2023).

Specific F-region irregularity events were presented and discussed by Rodrigues et al. (2023), and new case studies will be presented and discussed at a later time. Here, we present and discuss results related to statistical analyses of the nighttime F-region observations made between August 2021 and February 2023.

The observations were made with an F-region mode that uses beams pointed in 10 different directions in the magnetic equatorial plane. While the pointing positions did change slightly throughout the period of interest, they are very similar to those listed in Table 1. Of main importance is that the system observes the F-region from the west of Jicamarca (~60º elevation) to the east (~60º elevation). Additionally, the finite beamwidth allows observations to be made perpendicular to the magnetic direction throughout the E- and F-region heights of interest. Therefore, coherent backscatter from field-aligned irregularities in the heights of interest is also possible.

Table 2 lists the main parameters of the radar mode used for the observations. We highlight that power (and signal-to-noise ratio - SNR) profiles are obtained every 2 seconds for each direction. We also point out that the inter-pulse period (IPP) changed from 973.5 km to 1,500 km on September 5, 2022, and the baud length changed from 3.0 km to 4.5 km on November 1, 2022. These changes were made to better synchronize the AMISR-14 experiment with other radar experiments at Jicamarca. These changes were considered in our analysis of the measurements and did not affect our interpretation. Finally, the observations analyzed in this study were made between approximately 18:00 local time (LT) and 07:00 LT of the following day. Therefore, the analyses include observations made in the pre- and post-midnight sectors.

Table 1 – AMISR-14 pointing directions.

Beam Number	Azimuth (degrees)	Elevation (degrees)
1	-95.2	59.5

2	-96.5	65.8
3	-97.7	73.8
4	-99.50	78.3
5	-108.4	86.6
6	102.5	85.1
7	93.2	80.4
8	90.00	74.00
9	90.00	66.2
10	88.9	61.2

Table 2 – AMISR-14 10-beam F-region experiment parameters.

Parameter	Jul. 22 – Sep. 4, 22	Sep. 5, 22 – Oc. 31, 22	Nov. 1, 22 - Ongoing
Frequency	445 MHz	445 MHz	445 MHz
Bragg wavelength	0.34 m	0.34 m	0.34 m
Panel configuration*	7 (N/S) x 2 (E/W)	7 (N/S) x 2 (E/W)	7 (N/S) x 2 (E/W)
Antenna HPBW (NS/EW)	1.4º (N/S) – 8.6º (E/W)	1.4º (N/S) – 8.6º (E/W)	1.4º (N/S) – 8.6º (E/W)
Nominal Peak power	~185 kW	~185 kW	~185 kW
Number of beam positions	10	10	10
Pulses per beam position	16	16	10
Inter-Pulse Period (IPP)	937.5 km	1500 km	1500 km
Code length	28 bauds	28 bauds	28 bauds
Baud length	3.0 km	3.0 km	4.5 km
Sampling	1.5 km	1.5 km	1.5 km
Coherent integration	None	None	None
Incoherent integration	320 (2 seconds)	200 (2 seconds)	200 (2 seconds)

* Panel configuration refers to how the 14 panels are placed. The configuration 7 (N/S) x 2 (E/W) refers to a rectangular configuration with 2 panels in the East-West direction and 7 panels in the North-South direction.

2.1.1 Analysis

In order to examine the occurrence of sub-meter F-region irregularities causing UHF echoes, we analyzed range-time-intensity (RTI) maps for each beam of the AMISR-14 F-region mode observations. A total of 288 observation days were available for this study.

For each day and each RTI map, we identified the occurrence of echoes caused by ionospheric irregularities. The analysis of the occurrence of echoes described here follows the approach used by Zhan et al. (2018) for JULIA measurements to produce a detection map for each RTI map. The detection map shows the occurrence (or absence) of irregularity-causing echoes as a function of local time and height.

Detection maps were determined based on the number of echoes above a threshold signal-to-noise ratio (SNR) within time versus height bins. These bins have a width of 5 minutes in LT and 15 km in height. A bin is marked with irregularity occurrence if it contains more than 50 echoes with SNR greater than -8 dB. The threshold SNR (-8 dB) and minimum number of echoes (50) were chosen to minimize the contamination of irregularity detection by interference from artificial sources.

Figure 1 illustrates the results of the generation of the detection maps. The panels on the left (Figure 1a) show the RTI maps for observations made on February 5, 2022. The panels correspond to west (top) and east (bottom) observations. Note that the observations, provided originally as a function

of range, are shown as a function of height taking into consideration the elevation angles of the antenna beams. The panels on the right (Figure 1b) show the detection maps with bins colored yellow indicating the detection of echoes and bins colored purple indicating the absence of echoes.
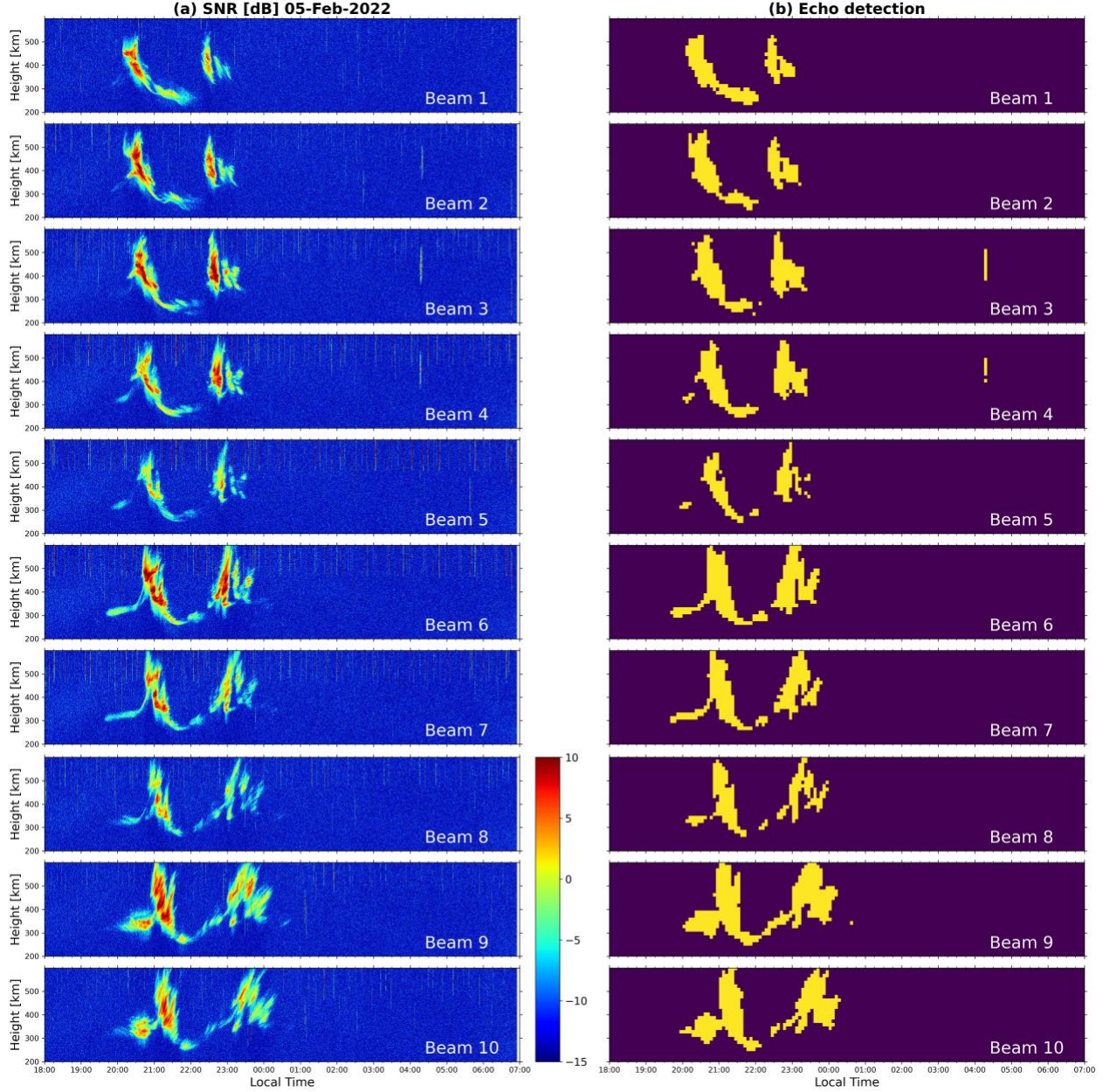

Figure 1. Illustration of the analyses performed in this study. (a) Panels on the left show RTI maps (LT vs height) of the observations made by the 10-beam AMISR-14 F-region mode on February 5, 2022. Beams from the west (top) to the east (bottom) are shown with the beam number indicated in each panel (see also Table 1). (b) Panels on the right show maps (LT vs height) indicating the occurrence (yellow) or absence (purple) of irregularity-causing echoes estimated using an approach similar to that applied by Zhan et al. (2018) and described in Section 2.1.1.

We point out the high occurrence of clutter caused by satellite echoes in the topside ionosphere or by meteor echoes coming through antenna sidelobes. The clutter can be seen in all RTI maps

(Figure 1a) as vertical streaks in SNR above approximately 400 km in height throughout the entire night. For completeness, we also show an example where clutter could not be avoided despite our filtering process. Clutter can be seen in the third and fourth beams of Figure 1b as a vertical streak of detections at approximately 04:00 LT. The false detection of irregularities does occur sporadically, but it does not affect the results presented and discussed in this report.

2.2 JULIA

In this study, we also used observations made by the JULIA radar configuration (Hysell and Burcham, 1998). JULIA is a low-power 50 MHz coherent scatter radar configuration that utilizes some of the antenna hardware of the Jicamarca incoherent scatter radar combined with low-power transmitters for routine, uninterrupted observations. For this study, we used the JULIA EW-ESF mode, which utilizes two beams in the magnetic equatorial plane to observe the occurrence of F-region echoes. The JULIA EW-ESF mode typically uses 5-baud coded pulses with 3.75 km bauds and an IPP of 937.5 km. Additionally, the peak power of the transmitter used is 8 kW. Two quarters of the 300 m x 300 m Jicamarca antenna are used for transmission, and two quarters are used for reception.

3 Results and Discussion

We now present and discuss the main results of our analyses of AMISR-14 F-region observations. We start with results related to LT and height variations in the occurrence rate of echoes for geomagnetically quiet conditions. The multi-beam observations allowed us to verify the variability in the occurrence rate of ESF for local zonal distances, that is, within a few 100s of km. We then present and discuss results related to the effects of solar flux conditions on the occurrence rates. Interpretation of AMISR-14 observations is then aided by observations made by the collocated VHF JULIA radar.

3.1 On quiet-time local zonal and seasonal variations

Here, we address how the climatology of sub-meter magnetic equatorial F-region irregularities, as observed by a UHF radar system, would vary with zonal distance and with changes in season. Using the echo detection maps described in the previous section, we computed maps of seasonal occurrence rates of the echoes associated with sub-meter irregularities. The occurrence rate is computed for each LT versus height bin.

Inspection of the data sets shows that, for a given day, the RTI maps for beams to the east could be very different from the RTI maps for beams to the west. An example of such a case is presented in Figure 2. Figure 2 shows the RTI maps for AMISR-14 observations made on March 6, 2022. This example shows that a radar plume develops over Jicamarca at around 20:00 LT and drifts to the east after that. While drifting to the east, the plume becomes more developed and robust, with stronger echoes observed in the easternmost beams (beams 9 and 10). During that time, between approximately 20:00 LT and 22:00 LT, only weak echoes associated with a bottom-type layer are observed by the beams pointed to the west (beams 1 to 5). The RTI maps in Figure 2 also show that, around 22:30 LT, echoes associated with another radar plume start to be observed in the westernmost beam (beam 1). This plume also drifts to the east but starts to decay while moving zonally. Only weak echoes are observed around Jicamarca (beams 5-7), and no echoes were detected in the easternmost beams (beams 8-10).
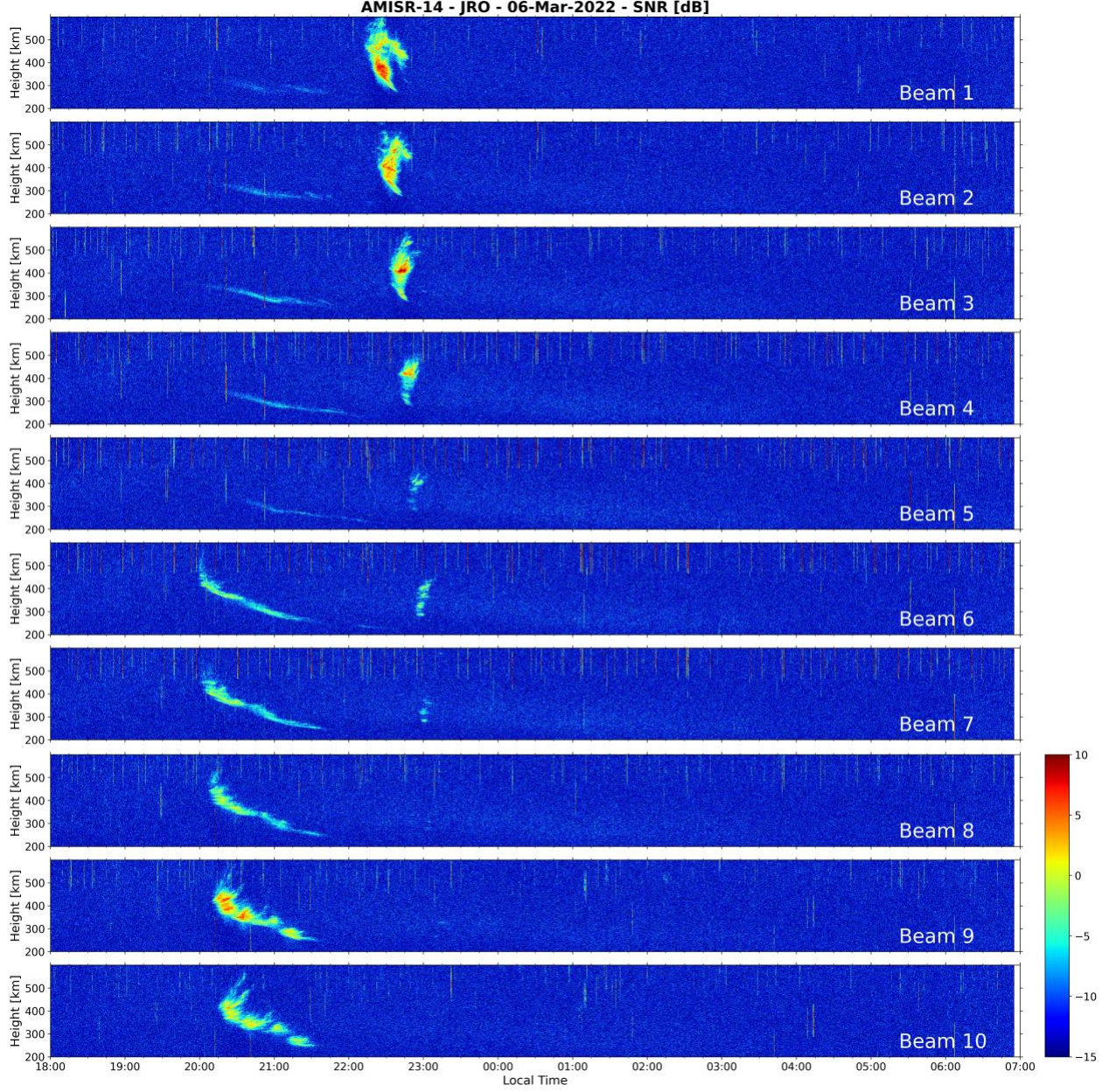
Figure 2. RTI maps for AMISR-14 observations made on March 6, 2022.

The example in Figure 2 shows that ESF development and occurrence on a given day are not evenly distributed over all the regions observed by the F-region experiment. More specifically, the example shows a post-sunset topside ESF event observed early in the evening to the east of Jicamarca and a late-evening topside ESF event first observed to the west of Jicamarca. This can be caused by zonal variations in ionospheric or thermospheric parameters (e.g., neutral winds, conductivities, vertical drifts) or by zonal variations in the availability of seed waves producing conditions that are favorable for the Generalized Rayleigh-Taylor (GRT) instability that is responsible for ESF (Sultan, 1996).

While zonal variations in ESF occurrence on a given night can be expected over zonal distances of a few 100s of km and are often seen in AMISR-14 observations, one could question whether

such zonal variations would also appear in climatological analyses. The semi-routine zonal observations made by AMISR-14 allow us to address this question. For that purpose, we analyzed seasonal variations in echo occurrence for each beam. The results are summarized in Figure 3.

Before discussing the results shown in Figure 3, we clarify that we only used observations made during geomagnetically quiet nights to obtain the F-region echo occurrence rates. Geomagnetic conditions for each observation were determined using the 3-hour geomagnetic Planetary K (Kp) index values. For an observation night to be considered geomagnetically quiet, all the Kp indices between 18:00 LT (23:00 UT) and 07:00 LT (12:00 UT) had to be less than 4. Additionally, to avoid as much as possible the effects of a disturbed dynamo, the previous four Kp values (between 09:00 UT and 21:00 UT) also had to remain below 4.

Each panel of Figure 3 shows the occurrence rate of F-region echoes as a function of LT and height for a specific pointing direction and season. Panel rows correspond to the same pointing direction. Panel columns correspond to the same season. The occurrence rates were computed as the fraction of the number of echo detections in each local time versus height bin over the total number of observation days in the relevant season. Observation days were grouped by season based on ± 45 days centered around 21 March (March equinox), 21 June (June solstice), 21 September (September equinox), and 21 December (December solstice). The total number of observation days, quiet days, and mean solar flux for each season are listed in Table 3. Before continuing, we point out that the echoes during December solstice 2022 around 200 km altitude are not F-region echoes. These echoes are clutter (code sidelobes) of nighttime E-region echoes. They are seen in the statistics for December 2022 because of the pulse length used during that time. Table 2 shows that on November 1, 2022, a longer coded pulse (4.5 km × 28 = 126 km) replaced the 84 km long pulse used until then.

The results in Figure 3 confirm the lack of any significant local zonal variability in the quiet-time occurrence rates for the local distances observed by AMISR-14. Considering the elevation and azimuth angles listed in Table 1, it can be shown that AMISR-14 observes the F-region at 350 km over a total zonal distance of approximately 400 km, from ~200 km to the west to ~200 km to the east. Effectively the same occurrence behaviors in time and height were found for different beams during the same season. Some of the small differences in the absolute occurrence rates can be attributed to distinct levels of interference and clutter for different pointing directions. The morphology of the post-midnight echoes is not as consistent, from beam to beam, as the morphology of pre-midnight echoes. This is because fewer cases of post-midnight events are observed in each season compared to pre-midnight events.

Table 3 - AMISR-14 observation days, quiet days, and average daily F10.7 index per season.
SFU stands for solar flux unit. 1 SFU = 10^{-22} W·m^{-2}·Hz^{-1}.

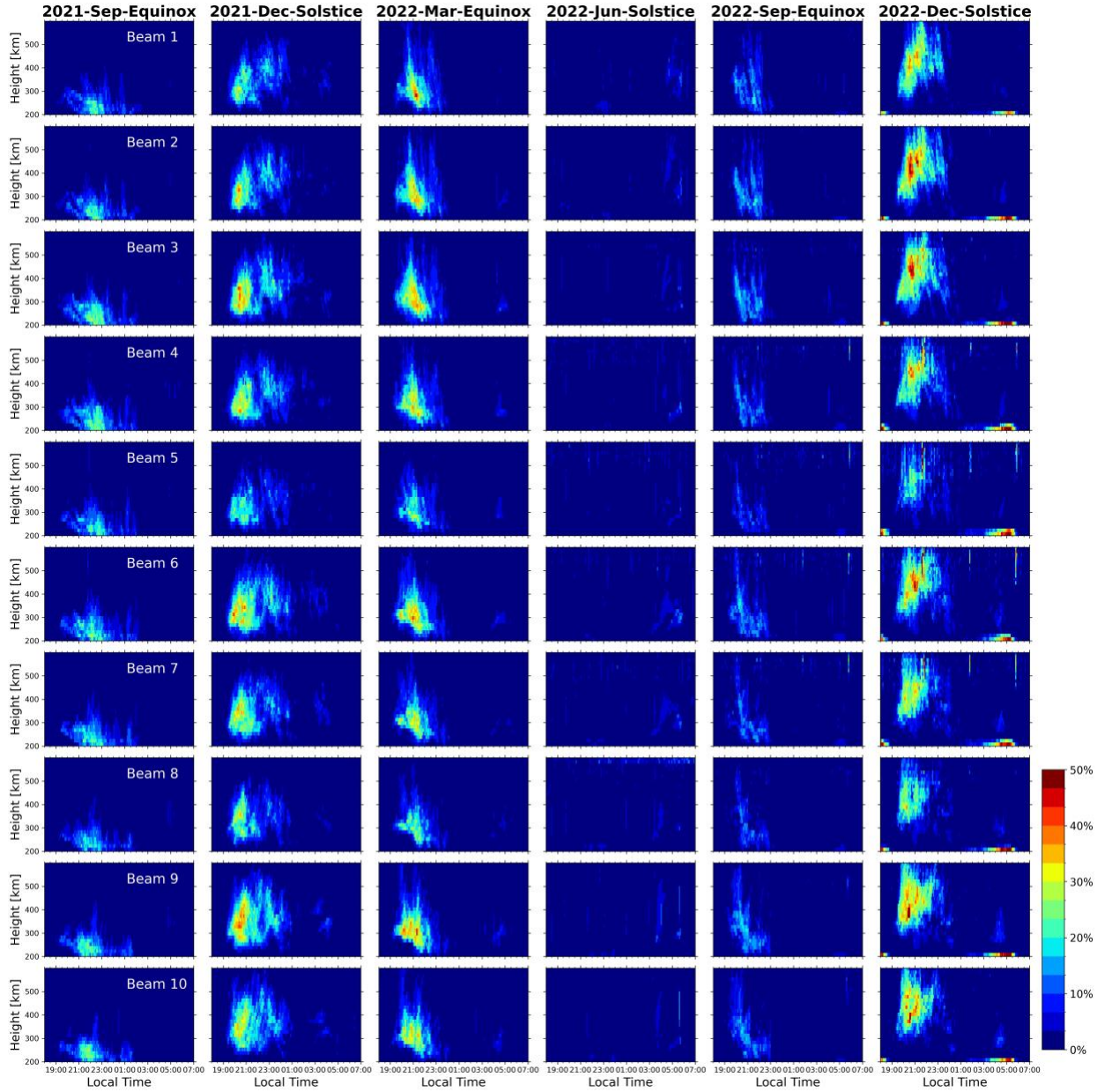| Season	Observation days (All)	Observation days (Quiet)	Average F10.7 (in SFU)
September equinox 2021	43	38	86.6
December solstice 2021	51	42	96.7
March equinox 2022	56	41	119.1
June solstice 2022	22	19	128.2
September equinox 2022	65	37	131.1
December solstice 2022	51	34	147.9

Figure 3. Occurrence rates (in %) of F-region echoes observed by AMISR-14 for different seasons and beams.

Figure 3 also shows a strong seasonal variation in the occurrence rates of F-region echoes. F-region echo occurrence rates reach maximum values during Equinox and December solstice. During June solstice, occurrence rates predominantly do not exceed 10%, a severe reduction compared to other seasons. As expected, the observed seasonal variations in the occurrence rates follow seasonal variations in quiet-time post-sunset ESF for the Peruvian sector (e.g., Abdu et al., 2000; Gentile et al., 2006; Zhan et al., 2018). Post-sunset ESF occurs predominantly during equinoxes and during December solstice when the evening pre-reversal enhancement (PRE) of the ionospheric vertical drifts is well-developed. During June solstice, however, the PRE in the Peruvian sector is weak, and ESF occurrence rates are reduced (Fejer et al., 1999).

13

Interesting features in the morphology of the seasonal occurrence rates of AMISR-14 echoes as a function of local time and height have also been identified. These features have been associated with solar flux and with the instrumentation used for this study and are discussed in the following sections.

3.2 On the observed effects of solar flux

Here, we address how the climatology of sub-meter magnetic equatorial F-region irregularities, as observed by a UHF radar system, would vary with changes in solar flux.

Figure 3 showed the expected seasonal variation in the occurrence of F-region echoes, which can be explained by seasonal variation in the occurrence of ESF in the Peruvian sector. Figure 3 results also showed features that can be associated with solar flux effects. One can see that the morphology of the occurrence rates changed significantly between repeated seasons: from September equinox 2021 to September equinox 2022 and from December solstice 2021 to December solstice 2022. Occurrence rates measured by beam 6 (close to vertical) for these seasons are shown again in Figure 4 for a side-by-side comparison. The average solar flux index (F10.7) is also indicated for each season.

Figure 4 shows that noticeable occurrence rates (approximately > 10%) reached higher altitudes in 2022 compared to observations in 2021. Results for September 2021 show that echoes occurred predominantly below 400 km. Results for September 2022, however, show noticeable occurrence rates reaching heights beyond 500 km.

A similar increase in altitude is evident in the December solstice results. Noticeable occurrence rates are seen predominantly above 500 km in the results for December 2022 and below 500 km for December 2021. While the differences in the pulse and IPP used for the observations in December solstice 2021 and December solstice 2022 might affect, to some degree, the estimated absolute occurrence rates, they do not affect the observed morphology of the occurrences, which is of main interest here. Figure 4 shows that echoes started at higher altitudes in 2022 compared with 2021 for both September equinox and December solstice.

The features described above can be associated with the increase in solar flux activity from 2021 to 2022. The average F10.7 index increased by more than 40 solar flux units (SFU) from September 2021 to September 2022 and more than 50 SFU from December 2021 to December 2022. Increases in solar flux lead to increases in the altitude of the bottomside equatorial F-region, where ESF structures are known to start. This explains the higher altitude of the initial echoes seen in 2022 (e.g., Chapagain et al., 2009; Smith et al., 2016).

Another subtle but interesting feature can be observed in the results for the repeated seasons. The results for September equinox show that during lower solar flux conditions (2021), F-region echoes can be observed until about 02:00 LT. During higher solar flux conditions (2022), however, echoes are observed only until about 23:00 LT. The same decrease in duration is shown for December solstice, where F-region echoes are observed until about 04:00 LT in 2021 and 01:00 LT in 2022. Zhan et al. (2018) credited the echo occurrences lasting longer during low solar flux

conditions to weaker (small amplitude) downward drifts that are more commonly observed during these conditions (Fejer et al., 1999; Smith et al., 2016). However, stronger downward drifts, which are observed more often during high solar flux conditions, would be stabilizing (Fejer et al., 1999). The stronger downward drifts would then produce less favorable conditions for instability growth as the night progresses. As a result, the occurrence of echoes would be more limited to the earlier hours at night during high solar flux conditions.
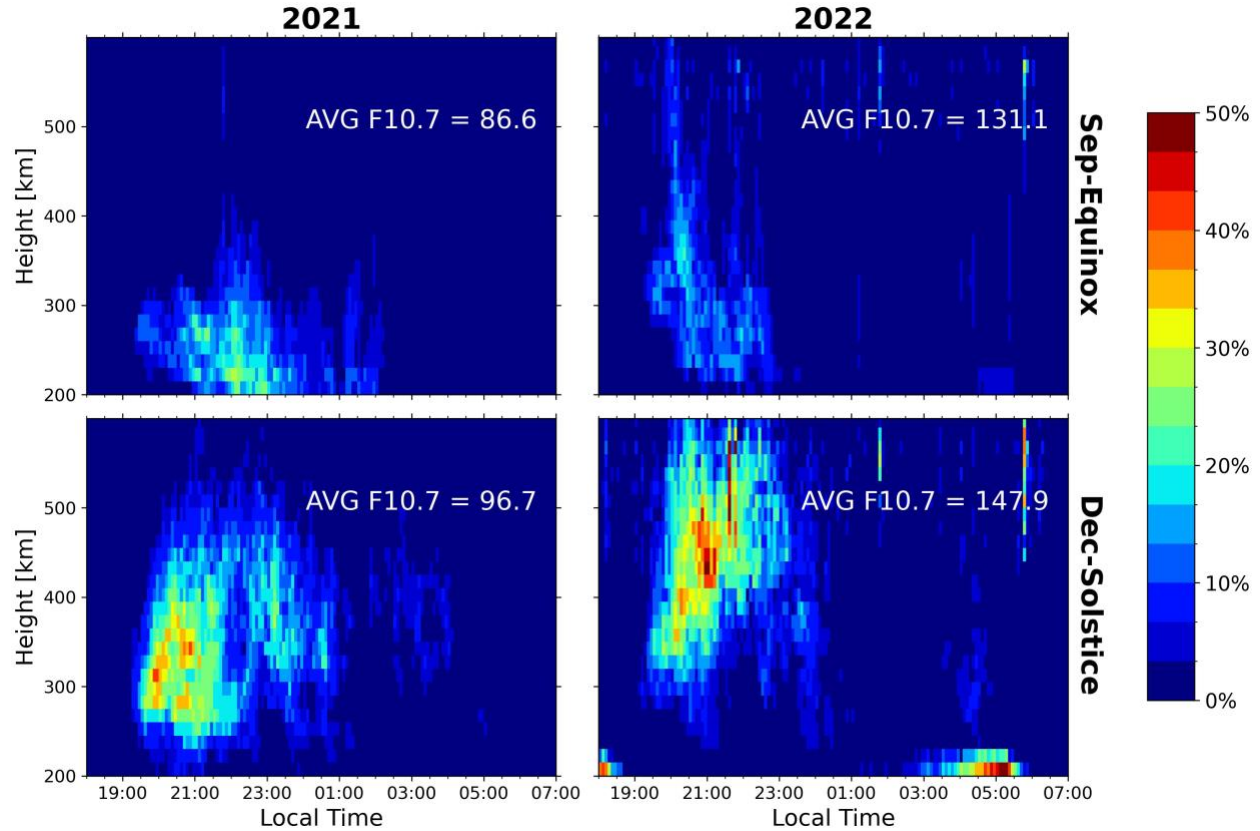

Figure 4 - Occurrence rates of F-region echoes observed by AMISR-14 (beam 6) during September equinox and December solstice in 2021 and 2022. The average F10.7 solar flux index during each season is indicated in each panel.

3.3 Comparisons with VHF observations by JULIA

A significant portion of our understanding of ESF comes from radar observations made over several decades at the JRO (e.g., Woodman and La Hoz, 1976; Woodman, 2009). These observations, however, have been made predominantly at 50 MHz and, therefore, measure echoes caused by Bragg scattering of irregularities with 3-meter scale sizes. AMISR-14, on the other hand, observes echoes from irregularities with scale sizes that are an order of magnitude smaller (0.34 m).

A more quantitative evaluation of same-day, collocated, dual-frequency observations made by JULIA and AMISR-14 will be presented and discussed in the future. We point out that differences can arise from many factors including pointing direction, pulse scheme, integration times, operating frequency, antenna pattern, etc. The contribution from some of these factors (e.g., pulse

scheme) can be reduced in future experiments. Here, however, we focus on the climatology that can be derived from the AMISR-14 observations that are already available and how this climatology compares with the climatology provided by JULIA measurements. Again, we highlight that this is important as we move forward with the development of new radar systems for geospace studies. For instance, if new UHF systems are developed for studies of low-latitude ionospheric irregularities, the results here provide a starting point to understand how UHF measurements compare to VHF measurements made in the past and/or at different longitude sectors.

For this comparison, we analyzed 179 days of observations made by JULIA between August 2021 and August 2022. The analyses of JULIA observations follow the procedure used for the analyses of AMISR-14 observations described in Section 2.1.1. As with the AMISR-14 RTI maps, the JULIA RTI maps were divided into local time versus height bins. The binning resolution was once again 5-minutes by 15 km in height. However, for JULIA RTI maps, a bin was considered to contain an irregularity if it contained more than 20 echoes with SNR greater than -20 dB. Additionally, following the same Kp criteria used to analyze the AMISR-14 observations, only geomagnetically quiet observations were used to analyze the JULIA measurements. Table 4 lists the number of observation days, the number of quiet days, and the mean F10.7 for each season.

Figure 5 shows the occurrence rates of F-region echoes as a function of LT and height for AMISR-14 (top row) and JULIA (bottom row) for different seasons (columns). AMISR-14 occurrence rates are for beam 6. The results show that the overall behavior of the occurrence rates derived from AMISR-14 observations matches well with the behavior estimated from JULIA observations for the four seasons shown in Figure 5. The AMISR-14 occurrence rates have similar altitudinal and temporal extents when compared with the ones of the JULIA occurrence rates. Also, both instruments show the expected seasonal variation of the F-region echo occurrence rates, with higher occurrence during Equinoxes and December solstice and severely reduced occurrence rates during June solstice. Both instruments even show the interesting occurrence of echoes between 04:00 LT and 06:00 LT during June solstice 2022.

We emphasize that, until now, there have been no reports, to our knowledge, describing the climatology of equatorial F-region echoes at UHF. We also highlight that the small differences between the UHF and VHF occurrence rates are impressively minimal despite the differences in the observational parameters (e.g., type of coded pulse, beam width) and the differences in the scale sizes of the irregularities observed. Additionally, in the four seasons presented in Figure 5, AMISR-14 and JULIA made simultaneous observations on only 89 geomagnetically quiet nights. Therefore, a little over one-third of the geomagnetically quiet JULIA observation days are different than the geomagnetically quiet AMISR-14 observation days.

We emphasize again that this finding is relevant for planning new observational capabilities. For instance, it provides a first look at what can be expected at UHF if new radars are to be developed to expand VHF measurements. It is also important if new UHF observations are to be compared with historical observations made by JULIA or other VHF systems.

While the overall morphology of the F-region occurrence rates observed by AMISR-14 and JULIA is similar, it is possible to see some small but noticeable differences. For instance, results in Figure

5 indicate higher VHF echo occurrence rates later in the night compared to UHF. This is more clearly seen in December solstice. The results in Figure 5 also indicate higher VHF echo occurrence rates at higher altitudes than UHF occurrence rates. Future experiments should be implemented to evaluate how much of these differences are due to differences in the observational parameters and to differences in the behavior of irregularities at different scale sizes.

Table 4 – Distribution of JULIA observations (per season) used in this study.

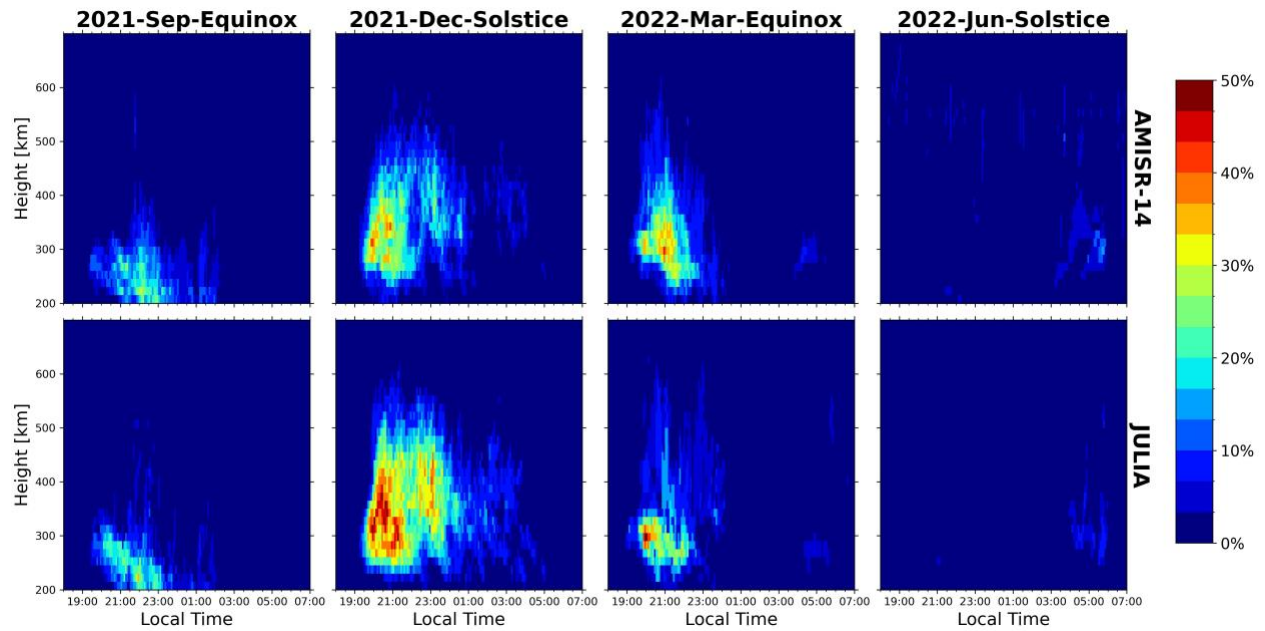| Season	Observation days (All)	Observation days (Quiet)	Average F10.7 (in SFU)
September equinox 2021	40	34	86.6
December solstice 2021	57	43	96.7
March equinox 2022	25	21	119.1
June solstice 2022	57	45	128.2

Figure 5. Dual-instrumented occurrence rates of F-region echoes observed between 7 August 2021 (± 45 days from 21 September) and 5 August 2022 (± 45 days from 21 June) grouped by season (column). The instrument used to obtain the results is indicated to the right of each row. Occurrence rates for AMISR-14 are for the observations with beam 6.

4 Conclusions

The deployment of AMISR-14 at the Jicamarca Radio Observatory provided an opportunity to conduct coherent backscatter radar observations of magnetic equatorial ionospheric irregularities at UHF. Until then, observations at Jicamarca and elsewhere have been made predominantly at VHF. VHF and UHF radars probe irregularities with scale sizes that are one order of magnitude apart. The 50 MHz JULIA radar probes irregularities with a scale size of 3-meters, while the 445 MHz AMISR-14 system probes irregularities with scale sizes around 0.34 meters.

Here, we use AMISR-14 semi-routine (~200 days per year) measurements made between August 2021 and February 2023 to determine, for the first time, how the climatology of UHF echoes (sub-meter irregularities) responds to changes in season and solar flux conditions. In addition, we take advantage of the two-dimensional AMISR-14 observations to determine variations, if any, in the climatology of the echoes over a zonal distance of about 400 km. Finally, we use AMISR-14 and JULIA observations to show how the UHF climatology compares with the collocated VHF climatology.

Our results provide the first look at the quiet-time climatology of nighttime F-region UHF echoes as a function of height and local time. Higher occurrence rates were observed during pre-midnight hours and during Equinox and December solstice. Reduced occurrence rates were observed during June solstice. This is in good agreement with previous studies of ESF in the Peruvian sector using different types of observations (e.g., Abdu et al., 2000; Gentile et al., 2006; Zhan et al., 2018). We point out that while one could have been inclined to suggest the relationship between UHF echoes and ESF, the analysis and results presented in this report quantify the UHF echo occurrence and provide experimental evidence of this relationship.

Furthermore, the observations also allowed us to determine the response of UHF F-region echoes to varying solar flux conditions. An increase in solar flux was followed by an increase in the altitude where noticeable occurrence rates ($\gtrsim$ 10%) start and in the maximum altitude of these occurrence rates. The observations also show that occurrence rates lasted longer (in LT) during low solar flux years. These findings are also in good agreement with previous studies (Chapagain et al., 2009; Hysell and Burcham, 2002) and with expectations for climatological variations in the nighttime equatorial F-region and in the equatorial vertical plasma drifts (e.g., Fejer et al., 1999; Kil et al., 2009; Smith et al., 2016; Zhan et al., 2018).

Comparisons with JULIA observations showed that despite differences in radar parameters, observation days, and scale sizes of the irregularities, the overall climatology derived from AMISR-14 and JULIA are very similar. This indicates that observations made by a UHF radar allow for a comparison with observations made by a VHF radar such as JULIA, at least from a climatological standpoint. This finding is important, for instance, if new UHF radar observational capabilities are to be created with the goal of expanding VHF measurements. It is also important if new UHF observations are to be compared with historical observations made by JULIA. Some small but noticeable differences between JULIA and AMISR-14 climatologies were identified. JULIA occurrence rates seemed to reach higher altitudes and last longer than AMISR-14

occurrence rates. Future radar experiments should be designed and carried out to investigate the relative contribution of observational parameters and irregularity scale sizes to these differences.

Finally, the analysis of ESF occurrence rates for different beams did not show any substantial variation over local (within a few 100s of km) zonal distances around JRO for any of the seasons and solar flux conditions. This indicates negligible climatological variations in factors controlling the development of ESF within a few 100s of km in zonal distance. We must point out, however, that observations on a single day do show strong local variations in echo detection and intensity within the AMISR-14 field of view due to the intrinsic development and decay of ESF structures.

Declarations

Availability of data and materials

The AMISR-14 data will be made available upon reasonable request to the corresponding author. The data are not yet publicly available due to being part of an ongoing PhD dissertation work.

The JULIA radar data is publicly available through the Madrigal online database (http://jro1.igp.gob.pe/madrigal/).

The geomagnetic Kp information was provided by the GFZ German Research Centre for Geosciences (https://kp.gfz-potsdam.de/en/).

The observed solar flux index (F10.7) information was provided by the National Research Council Canada in partnership with the Natural Resources Canada (https://www.spaceweather.gc.ca/).

Declaration of interests

The authors declare that they have no competing interests.

Funding

Authors' contributions

AAM contributed with the analysis of the observations, the interpretation of the results, and the writing of the manuscript. FSR proposed the study, provided guidance for the analysis of the measurements, and contributed to the interpretation of the results and writing. JS contributed to the interpretation of the observations and editing of the manuscript.

DS, MM, JMA, and KMK contributed with tasks related to operations and repairs of AMISR-14 and the design of the radar experiments. CP contributed with the instrumentation (AMISR-14) used in this study.

Acknowledgments

References

Abdu, M. A., Sobral J. H. A., and Batista, I. S. (2000), Equatorial spread F statistics in the American longitudes: Some problems relevant to ESF description in the IRI scheme, Adv. in Space Res., 25(1), 113-124, doi:10.1016/S0273-1177(99)00907-2.

Abdu, M.A. (2019), Day-to-day and short-term variabilities in the equatorial plasma bubble/spread F irregularity seeding and development, Prog. Earth Planet. Sci., 6(11), doi:10.1186/s40645-019-0258-1.

Alfonsi, L., Spogli, L., Pezzopane, M., Romano, V., Zuccheretti, E., De Franceschi, G., Cabrera, M. A., and Ezquer, R. G. (2013), Comparative analysis of spread-F signature and GPS scintillation occurrences at Tucumán, Argentina, J. Geophys. Res. Space Phys., 118, 4483–4502, doi:10.1002/jgra.50378.

Booker, H. G. and Wells, H. W. (1938), Scattering of radio waves by the F region of the ionosphere, J. Geophys. Res., 43(3), 249–256, doi:10.1029/TE043i003p00249.

Carrano, C. S., and Groves, K. M. (2007), TEC Gradients and Fluctuations at Low, Latitudes Measured With High Data Rate GPS Receivers, Proceedings of the 63rd Annual Meeting of The Institute of Navigation, Cambridge, MA, 156-163.

Chapagain, N. P., Fejer B. G., and Chau J. L. (2009), Climatology of postsunset equatorial spread F over Jicamarca. J. Geophys. Res. Space Phys., 114(A7), doi:10.1029/2008JA013911.

Chau, J. L., and Woodman, R. F. (2001), Three-dimensional coherent radar imaging at Jicamarca: Comparison of different inversion techniques, J. Atmos. Sol. Terr. Phys., 63(2-3), 253–261, doi:10.1016/S1364-6826(00)00142-5.

Fejer, B. G., Scherliess, L., and de Paula, E. R. (1999), Effects of the vertical plasma drift velocity on the generation and evolution of equatorial spread F, J. Geophys. Res., 104(A9), 19859– 19869, doi:10.1029/1999JA900271.

Gentile, L. C., Burke, W. J., and Rich, F. J. (2006), A climatology of equatorial plasma bubbles from DMSP 1989–2004, Radio Sci., 41, RS5S21, doi:10.1029/2005RS003340.

Harding, B. J., and Milla, M. (2013), Radar imaging with compressed sensing, Radio Sci., 48, 582–588, doi:10.1002/rds.20063.

Hickey, D. A., Martinis, C. R., Rodrigues, F. S., Varney, R. H., Milla, M. A., Nicolls, M. J., Strømme, A., Arratia, J. F. (2015), Concurrent observations at the magnetic equator of small-scale irregularities and large-scale depletions associated with equatorial spread F, J. Geophys. Res. Space Physics, 120, doi:10.1002/2015JA021991.

Hoegy, W. R., Curtis, S. A., Brace, L. H., Maynard, N. C., Heelis, R. A. (1982), Dynamics Explorer observations of equatorial spread F: Evidence for drift waves, Geophys. Res. Lett., 9(9), 993-996, doi:10.1029/GL009i009p00993.

Hysell, D. L. (1996), Radar imaging of equatorial F region irregularities with maximum entropy interferometry, Radio Sci., 31(6), 1567–1578, doi:10.1029/96RS02334.

Hysell, D. L., and Burcham, J. D. (1998), JULIA radar studies of equatorial spread F, J. of Geophys. Res., 103(A12), 29155–29167, doi:10.1029/98JA02655.

Hysell, D. L., and Burcham, J. D. (2002), Long term studies of equatorial spread F using the JULIA radar at Jicamarca, J. Atmos. Sol. Terr. Phys., 64(12–14), 1531–1543, doi:10.1016/S1364-6826(02)00091-3.

Hysell, D. L., Chau, J. L., Coles, W. A., Milla, M., Obenberger, K., and Vierinen, J. (2019), The case for combining a large low-band Very High Frequency transmitter with multiple receiving arrays for geospace research: A geospace radar. Radio Sci., 54, 533–551, doi:10.1029/2018RS006688.

Jahn, J. M., and LaBelle, J. (1998), Rocket measurements of high-altitude spread F irregularities at the magnetic dip equator, J. Geophys. Res., 103(A10), 23427–23441, doi:10.1029/97JA02636.

Kelley, M. C., Makela, J. J., Ledvina, B. M., and Kintner, P. M. (2002), Observations of equatorial spread-F from Haleakala, Hawaii, Geophys. Res. Lett., 29(20), doi:10.1029/2002GL015509.

Kil, H., Paxton, L. J., and Oh, S. J. (2009), Global bubble distribution seen from ROCSAT-1 and its association with the evening prereversal enhancement, J. Geophys. Res., 114, A06307, doi:10.1029/2008JA013672.

Kudeki, E., and Sürücü, F. (1991), Radar interferometric imaging of field-aligned plasma irregularities in the equatorial electrojet, Geophys. Res. Lett., 18(1), 41–44, doi:10.1029/90GL02603.

Martinis, C., and Mendillo, M. (2007), Equatorial spread F-related airglow depletions at Arecibo and conjugate observations, J. Geophys. Res., 112, A10310, doi:10.1029/2007JA012403.

Otsuka, Y. (2018), Review of the generation mechanisms of post-midnight irregularities in the equatorial and low-latitude ionosphere, Prog. Earth Planet. Sci., 5(57), doi:10.1186/s40645-018-0212-7.

Patra, A. K., Phanikumar, D. V., Pant, T. K. (2009), Gadanki radar observations of F region field-aligned irregularities during June solstice of solar minimum: first results and preliminary analysis, J. Geophys. Res., 114, A12305, doi:10.1029/2009JA014437.

Rastogi, R. G., Mullen, J. P., and MacKenzie, E. (1981), Effect of geomagnetic activity on equatorial radio VHF scintillations and spread F, J. Geophys. Res., 86(A5), 3661–3664, doi:10.1029/JA086iA05p03661.

Rino, C. L., Tsunoda, R. T., Petriceks, J., Livingston, R. C., Kelley, M. C., and Baker, K. D. (1981), Simultaneous rocket-borne beacon and in situ measurements of equatorial spread F—Intermediate wavelength results, J. Geophys. Res., 86(A4), 2411–2420, doi:10.1029/JA086iA04p02411.

Rodrigues, F. S., de Paula, E. R., Abdu, M. A., Jardim, A. C., Iyer, K. N., Kintner, P. M., and Hysell, D. L. (2004), Equatorial spread F irregularity characteristics over São Luís, Brazil, using VHF radar and GPS scintillation techniques, Radio Sci., 39, RS1S31, doi:10.1029/2002RS002826.

Rodrigues, F. S., Kelley, M. C., Roddy, P. A., Hunton, D. E., Pfaff, R. F., de La Beaujardière, O., and Bust, G. S. (2009), C/NOFS observations of intermediate and transitional scale-size equatorial spread F irregularities, Geophys. Res. Lett., 36, L00C05, doi:10.1029/2009GL038905.

Rodrigues, F. S., Nicolls, M. J., Milla, M. A., Smith, J. M., Varney, R. H., Strømme, A., Martinis, C., and Arratia, J. F. (2015), AMISR-14: Observations of equatorial spread F, Geophys. Res. Lett., 42, 5100–5108, doi:10.1002/2015GL064574.

Rodrigues, F. S., de Paula, E. R., and Zewdie, G. K. (2017) High-resolution coherent backscatter interferometric radar images of equatorial spread F using Capon's method, Ann. Geophys., 35, 393-402, doi:10.5194/angeo-35-393-2017.

Rodrigues, F. S., Milla, M. A., Scipion, D., Apaza, J. M., Kuyeng, K. M., Sousasantos, J., Massoud, A. A., and Padin, C. (2023), On new two-dimensional UHF radar observations of equatorial spread F at the Jicamarca Radio Observatory, Earth Planets Space, 75(120), doi:10.1186/s40623-023-01876-7.

Sekar, R., Chakrabarty, D., Narayanan, R., and Patra, A. K. (2008), Equatorial Spread F structures and associated airglow intensity variations observed over Gadanki, Ann. Geophys., 26, 3863–3873, doi:10.5194/angeo-26-3863-2008.

Smith, J. M., Rodrigues, F. S., Fejer, B. G., and Milla, M. A. (2016), Coherent and incoherent scatter radar study of the climatology and day-to-day variability of mean F region vertical drifts and equatorial spread F, J. Geophys. Res. Space Physics, 121, 1466–1482, doi:10.1002/2015JA021934.

Sultan, P. J. (1996), Linear theory and modeling of the Rayleigh-Taylor instability leading to the occurrence of equatorial spread F, J. Geophys. Res., 101(A12), 26875–26891, doi:10.1029/96JA00682.

Szuszczewicz, E. P., Tsunoda, R. T., Narcisi, R., and Holmes, J. C. (1980), Coincident radar and rocket observations of equatorial spread-F. Geophys. Res. Lett., 7, 537-540. doi:10.1029/GL007i007p00537.

Thampi, S. V., Yamamoto, M., Tsunoda, R. T., Otsuka, Y., Tsugawa, T., Uemoto, J., and Ishii, M. (2009), First observations of large-scale wave structure and equatorial spread F using CERTO radio beacon on the C/NOFS satellite, Geophys. Res. Lett., 36, L18111, doi:10.1029/2009GL039887.

Tsunoda, R. T. (2006), Day-to-day variability in equatorial spread F: Is there some physics missing?, Geophys. Res. Lett., 33, L16106, doi:10.1029/2006GL025956.

Valentic T. et al. (2013), AMISR the advanced modular incoherent scatter radar, Proc. IEEE Int. Symp. Phased Array Syst. Technol., 659-663, doi:10.1109/ARRAY.2013.6731908.

Woodman, R. F., and La Hoz, C. (1976), Radar observations of F region equatorial irregularities, J. Geophys. Res., 81(31), 5447–5466, doi:10.1029/JA081i031p05447.

Woodman, R. F. (2009), Spread F – an old equatorial aeronomy problem finally resolved?, Ann. Geophys., 27, 1915–1934, doi:10.5194/angeo-27-1915-2009.

Yizengaw, E., Retterer, J., Pacheco, E. E., Roddy, P., Groves, K., Caton, R., and Baki, P. (2013), Postmidnight bubbles and scintillations in the quiet-time June solstice, Geophys. Res. Lett., 40, 5592–5597, doi:10.1002/2013GL058307.

Zhan, W., Rodrigues, F., and Milla, M. (2018), On the genesis of postmidnight equatorial spread F: Results for the American/Peruvian sector, Geophys. Res. Letters, 45, 7354–7361. doi:10.1029/2018GL078822.